Biomineralization

- ## Types & Uses

  - ### Calcium carbonate
    - Calcite & Aragonite (shells, lenses, gravity sensors)
    - Vaterite (inner ear of two types of fish)
      & Amorphous phases (Ca storage spindles in plants)
  - ### Calcium phosphate (bones, teeth)
  - ### Other Group 2A elements
  - ### Silica (diatom & radiolarian micro shells)
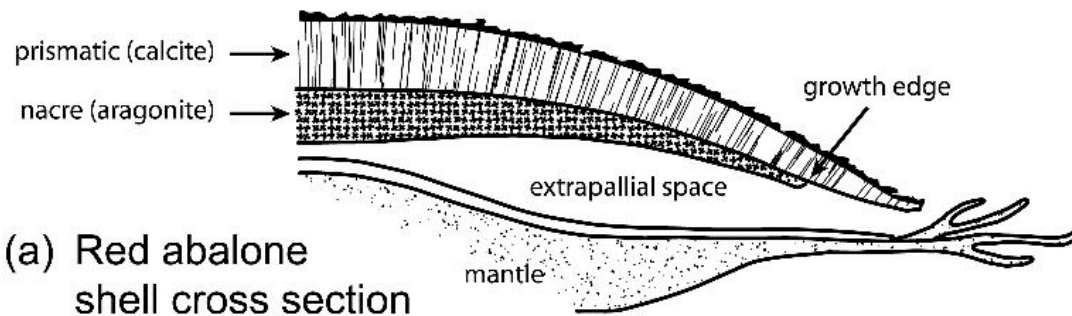 - ### Iron oxides
  - ### Metal sulfides

- ## While organic components may be only a few %, they are critical to the important properties of the materials.
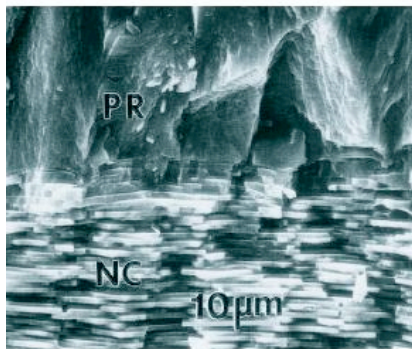
Calcium carbonate

Mineral	Formula	Organism	Location	Function
Calcite	$CaCO_3$	Foraminifera	Shell	Exoskeleton
		Trilobite	Eye lens	Optics
		Molluscs	Shell	Exoskeleton
		Crustaceans	Crab cuticle	Mechanical strength
		Birds	Eggshells	Protection
		Mammals	Inner ear	Gravity receptor
Mg-calcite	$(Mg,Ca)CO_3$	Octocorals	Spicules	Mechanical strength
		Echinoderms	Shells/spines	Protection
Aragonite	$CaCO_3$	Corals	Cell wall	Exoskeleton
		Molluscs	Shell	Exoskeleton
		Gastropods	Love dart	Reproduction
		Cephalopods	Shell	Buoyancy
		Fish	Head	Gravity receptor
Valerite	$CaCO_3$	Gastropods	Shell	Exoskeleton
		Ascidians	Spicules	Protection
Amorphous	$CaCO_3 \cdot H_2O$	Crustateans	Crab cuticle	Mechanical strength
		Plants	Leaves	Calcium storage

Different forms of CaCO$_3$

prismatic (calcite)

nacre (aragonite)

growth edge

(a) Red abalone shell cross section

extrapallial space

mantle

PR

NC

10µm

(b)

[001]

[001]

[110]

(c)

y

z

x

2Θ

q$_{HK0}$

θ

(d)

- **Calcite (prismatic)**
  - Hardness
- **Aragonite (nacre)**
  - Toughness
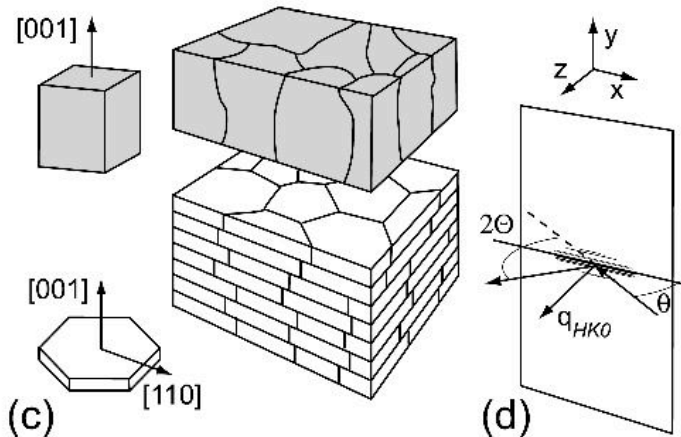
www.solids.bnl.gov/ ~dimasi/bones/abalone/

Nacre layers

Nacre layer on a pearl

organic layer (conchiolin)

CaCO3 (aragonite crystals)

Geology 306
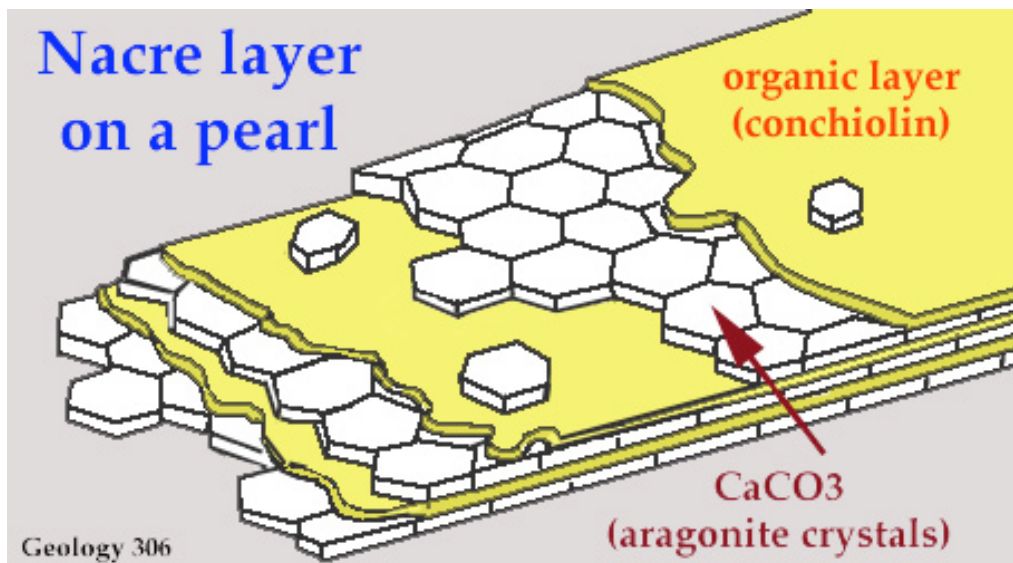
- Aragonite polygonal tablets (500 nm thick).
- Protein/polysaccharide organic matrix (30 nm thick).

Calcium phosphate

- Hydroxyapatite $Ca_{10}(PO_4)_6(OH)_2$ Vertebrates   Bone
-   Mammals   Teeth
-   Fish   Scales
- Octacalcium phosphate   Vertebrates
-                 $Ca_8H_2(PO_4)_6$ Bone/teeth precursor
- Amorphous   various   Chitons   Teeth
-   Gastropods   Gizzard plates
-   Mammals   Milk (ion storage)

Hydroxyapatite can also contain Sr, Mg, Na, CO_3, etc.

Levels of bone structure
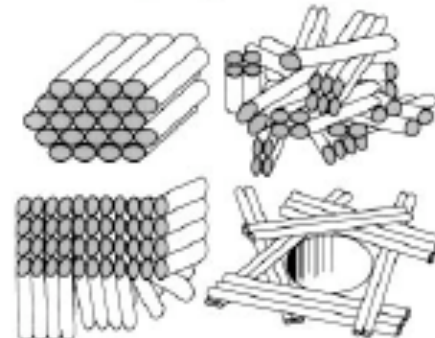
Hydroxyapatite:
Crystalline calcium phosphate
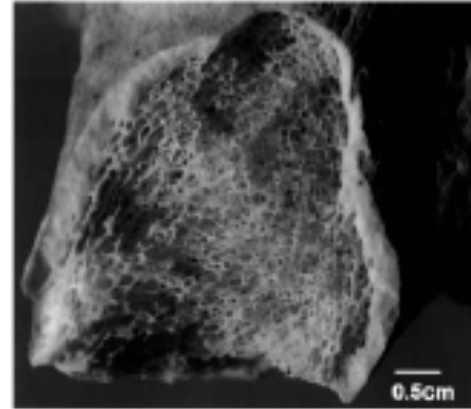
Level 7: Whole Bone

Level 6: Spongy vs Compact Bone
0.5cm

Level 5: Cylindrical Motifs: Osteons
10μm

Level 4: Fibril Array Patterns

Level 3: Fibril Array
200nm
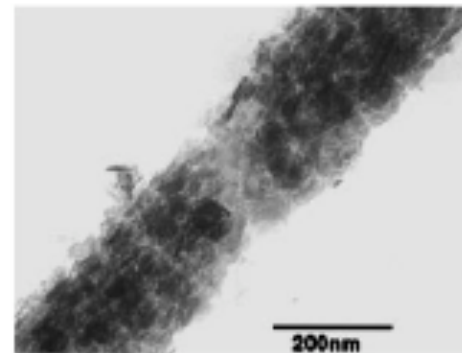
Level 2: Mineralized Collagen Fibril
200nm
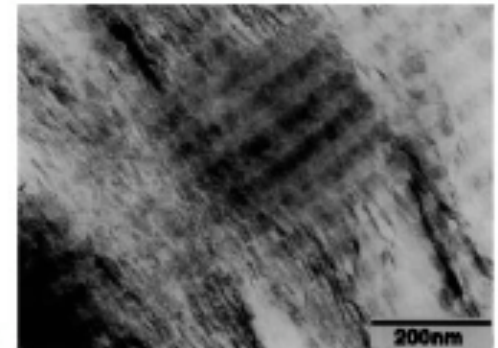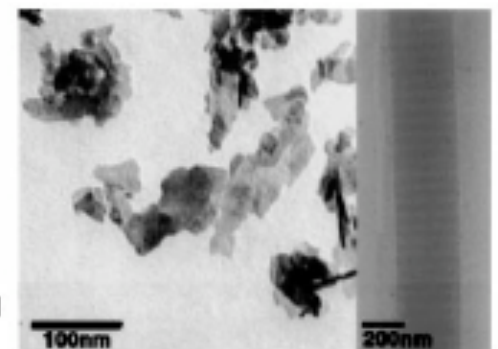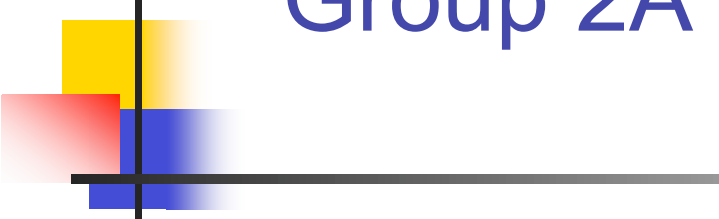
Level 1: Major Components
100nm   200nm

Group 2A

- Gypsum $CaSO_4 \cdot 2H_2O$ Jellyfish gravity receptor
- Celestite $SrSO_4$ Acantharia micro-skeleton
- Barite $BaSO_4$ Loxedes gravity receptor

Magnetosomes in Bacteria

U. Heyen & D. Schler Growth and magnetosome formation by microaerophilic
Magnetospirillum strains in an oxygen-controlled fermentor   Appl Microbiol
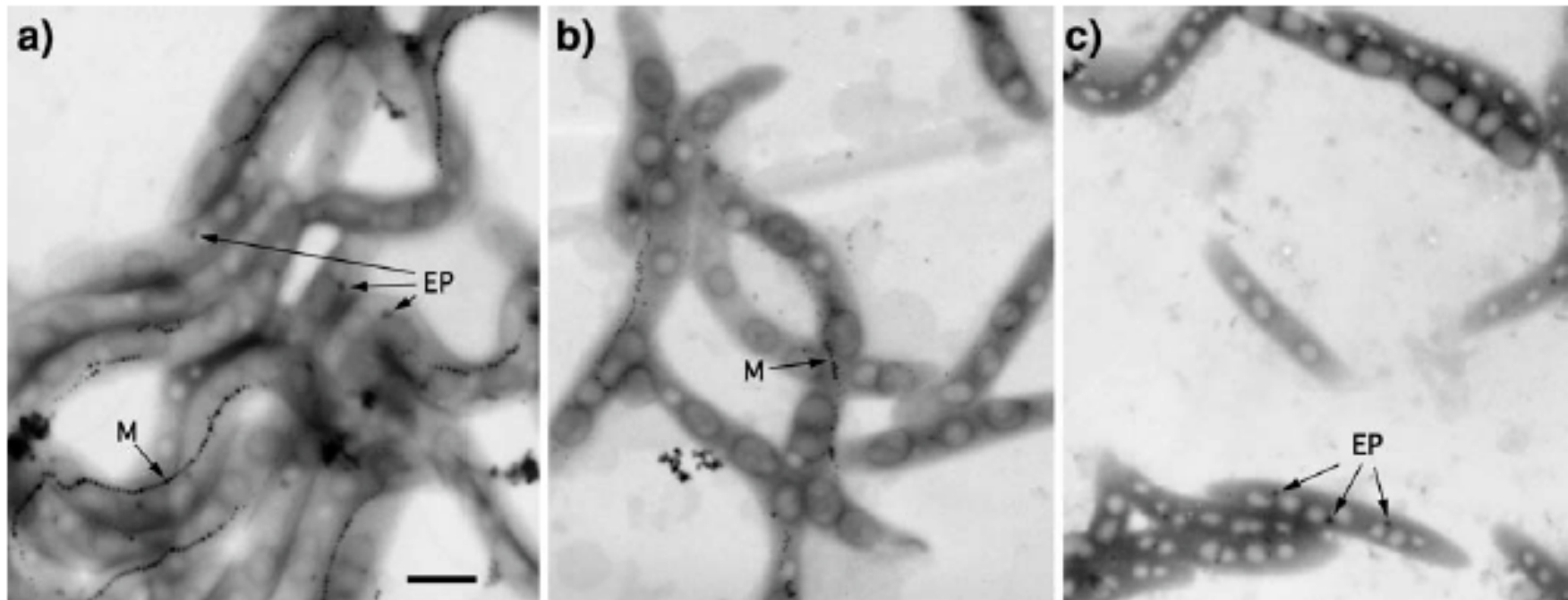Biotechnol (2003) 61:536–544

Fig. 3a–c Electron micrographs of *M. gryphiswaldense* cultures grown in the oxystat at defined pO_2 tensions of 0.25 mbar (a), 10 mbar (b), and 20 mbar (c). *Arrows* indicate the magnetosome chains (*M*) and the electron-dense particles (*EP*) found in magnetic and non-magnetic cells. The bright inclusions represent polyhydroxyalkanoate globules. *Bar* 0.5 μm

Magnetosomes in Bacteria

(scale bars = 100 nm)

http://magnum.mpi-bremen.de/magneto/

4/25/06   LaBean COMPSCI 296.5
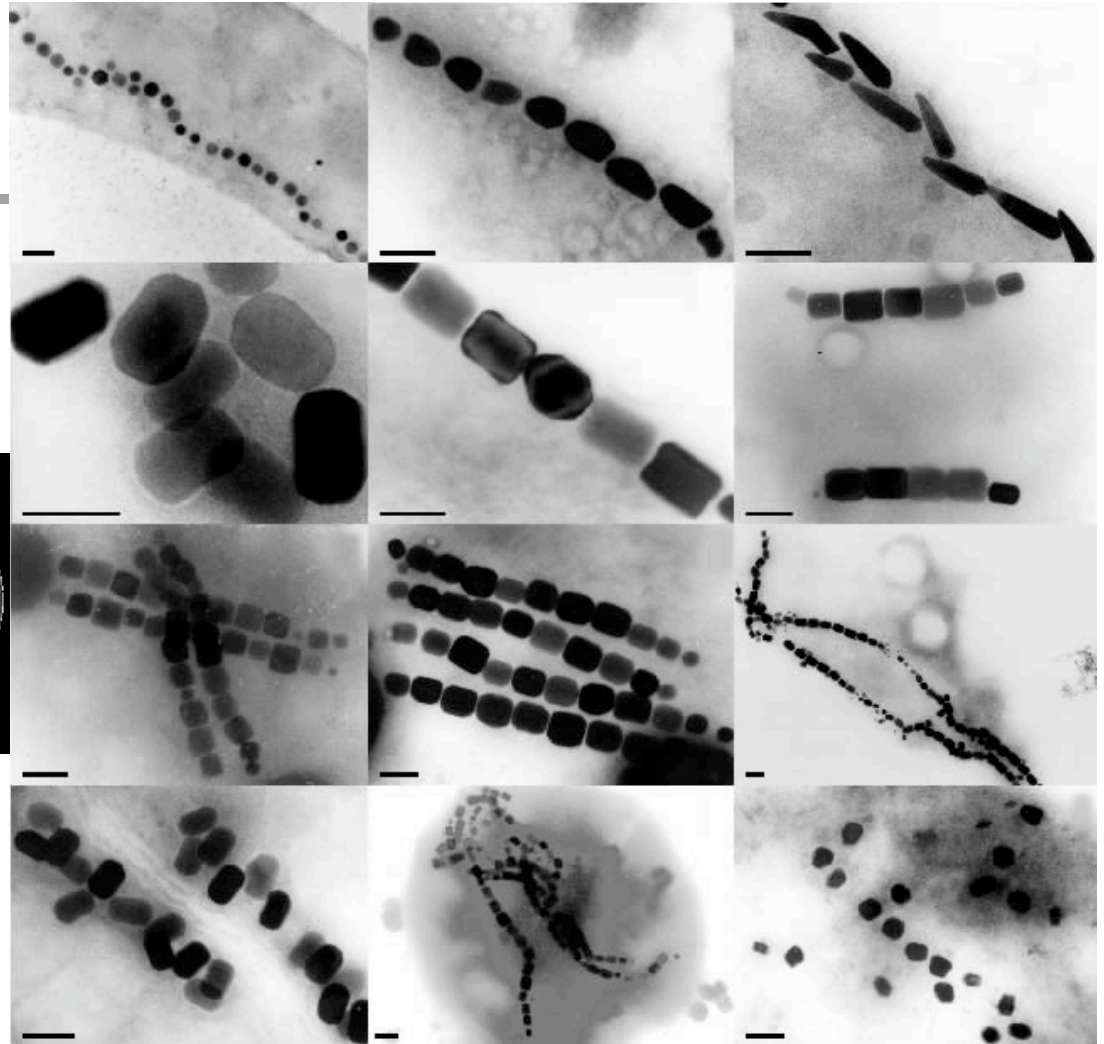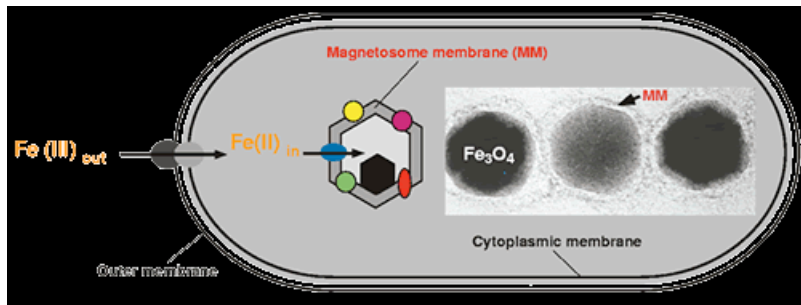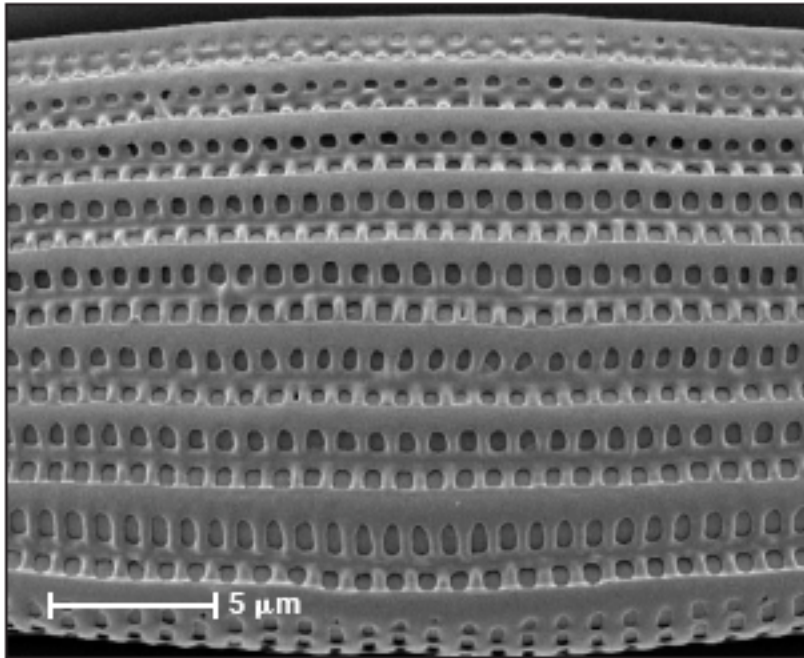
Intricate walls. Scanning electron micrograph of the silica wall of the marine benthic diatom *Amphora coffeae-formis.* Note the ornate structure, patterning, and porosity of the silica wall.
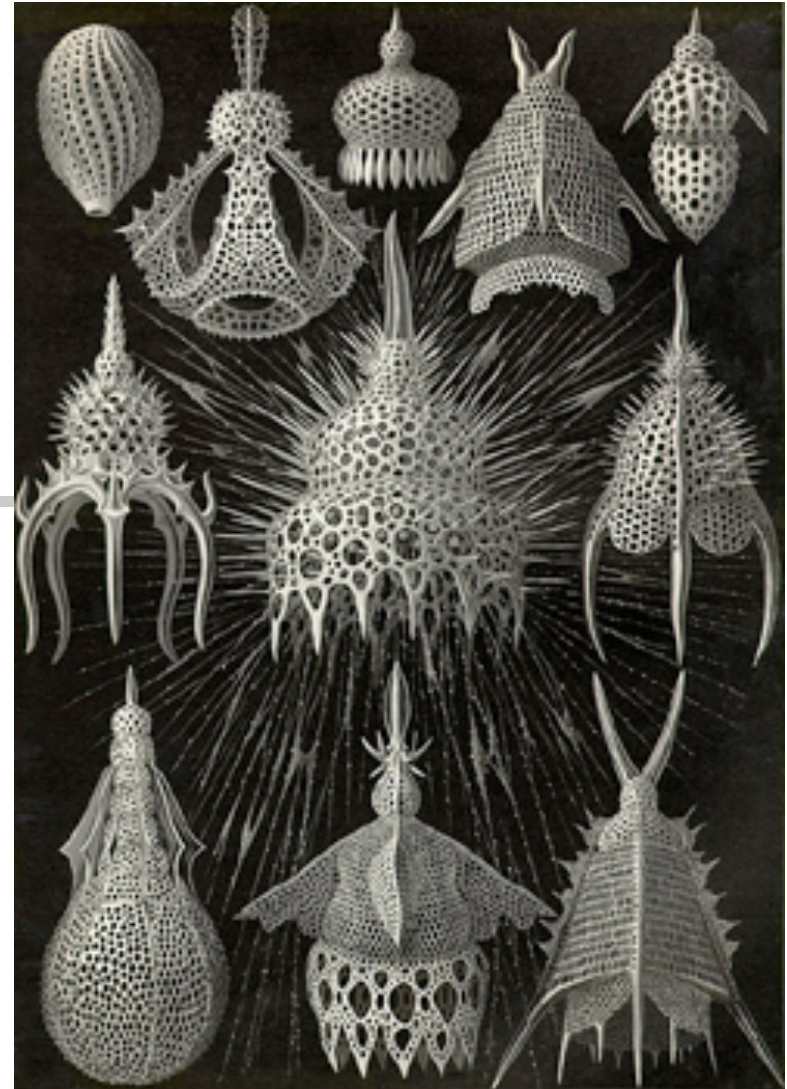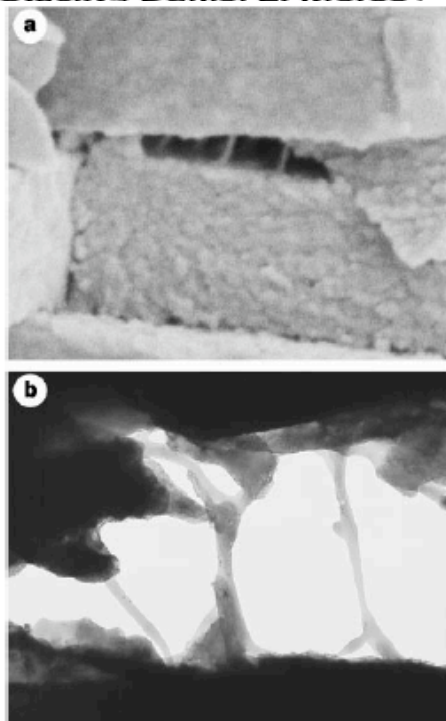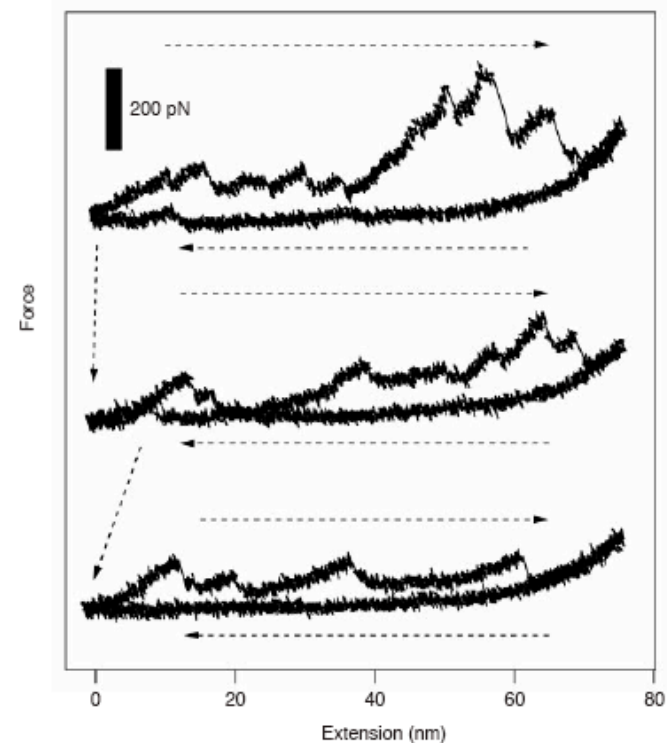

4/25/06

Molecular mechanistic origin of the toughness of natural adhesives, fibres and composites

Bettye L. Smith*†, Tilman E. Schäffer‡†, Mario Viani*,
James B. Thompson*, Neil A. Frederick*, Johannes Kindt*,
Angela Belcher§, Galen D. Stucky∥, Daniel E. Morse¶
& Paul K. Hansma*

Figure 1 Scanning and transmission electron micrographs of a freshly cleaved abalone shell, showing adhesive ligaments formed between nacre tablets. **a**, Scanning electron micrograph of a freshly cleaved abalone shell showing adhesive ligaments formed between consecutive abalone nacre tablets on exertion of mechanical stress. The tablets are ~400 nm thick. **b**, Transmission electron micrograph of another cleaved abalone shell, showing the adhesive ligaments between nacre tablets. The space between the tablets is ~600 nm. Thus the ligaments can lengthen to many times the original spacing between the tablets, which is of the order of 30 nm.

Figure 2 Consecutive force–extension curves, obtained using an atomic force microscope, from pulling on a freshly cleaved abalone nacre surface. Rupture events, with a sawtooth appearance, are visible in each of the curves. The surface was not touched between pulls, strong evidence that some refolding took place, possibly of domains in lustrin A. The approach and retract curves show hysteresis, indicating that the rupture events dissipate energy.

4/25/06

Molecular mechanistic origin of the toughness of natural adhesives, fibres and composites

Bettye L. Smith*†, Tilman E. Schäffer‡†, Mario Viani*,
James B. Thompson*, Neil A. Frederick*, Johannes Kindt*,
Angela Belcher§, Galen D. Stucky‖, Daniel E. Morse¶
& Paul K. Hansma*
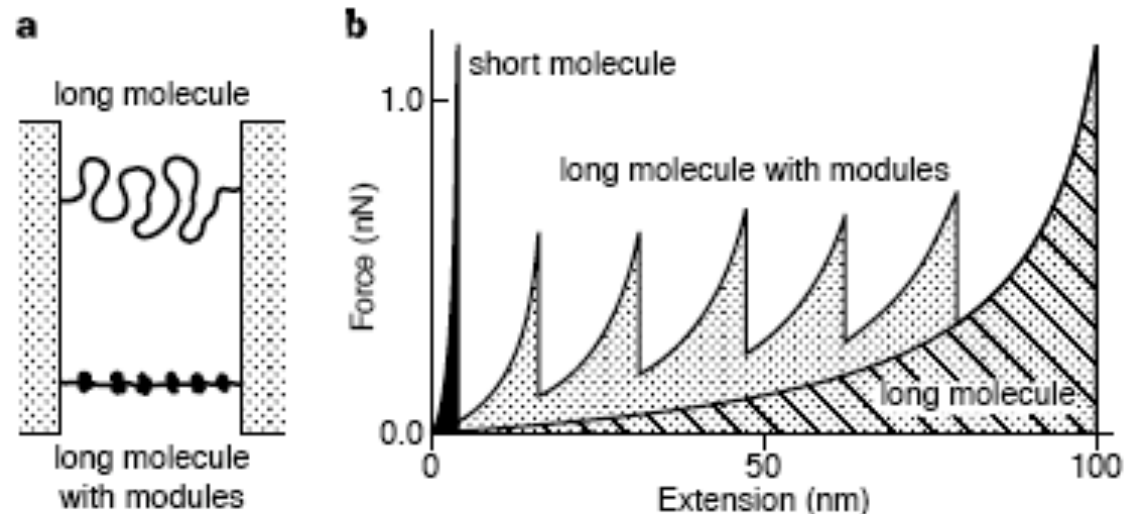
Figure 3 Model of long polymers and force–extension curves for different kinds of polymers. **a**, Diagram of long polymers behaving as entropic springs. The lower molecule is compacted, with many domains that are held together with intermediate-strength sacrificial bonds. **b**, Force–extension curves for three different kinds of molecules. A short molecule (solid curve) resists pulling up to a high force before

Self-Assembly and Mineralization of Peptide-Amphiphile Nanofibers

Jeffrey D. Hartgerink, Elia Beniash, Samuel I. Stupp*

- Peptide-amphiphile
- pH induced self-assembly
- Fibrous scaffold
  - Like "extracellular matrix"
  - Reversible cross-links for switch stabilization
- Composite formed by hydroxyapatite mineralization
  - some what similar to bone
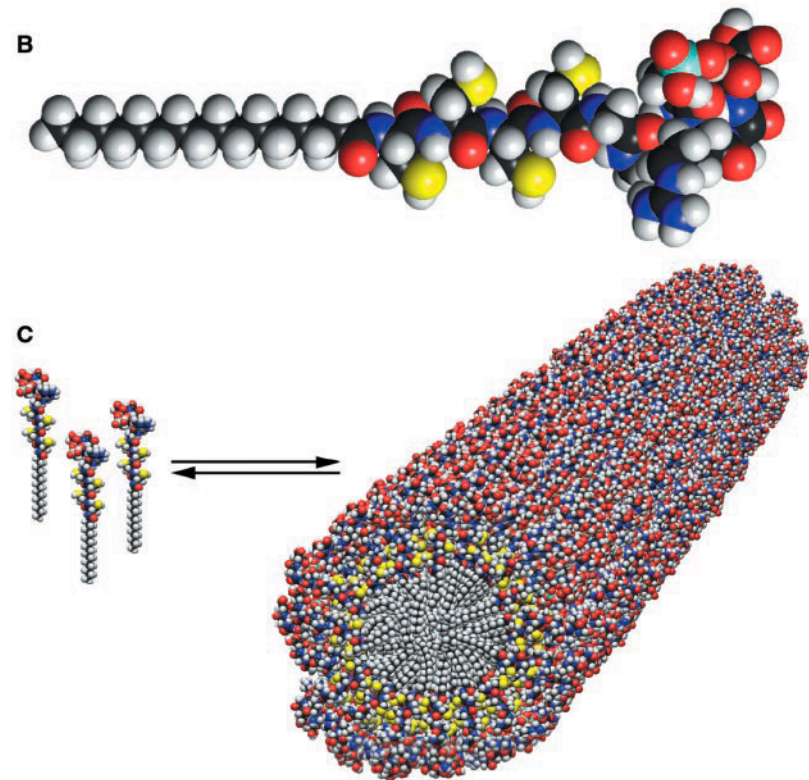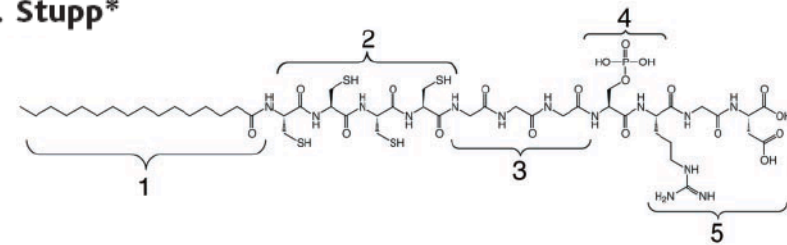
Mineralization
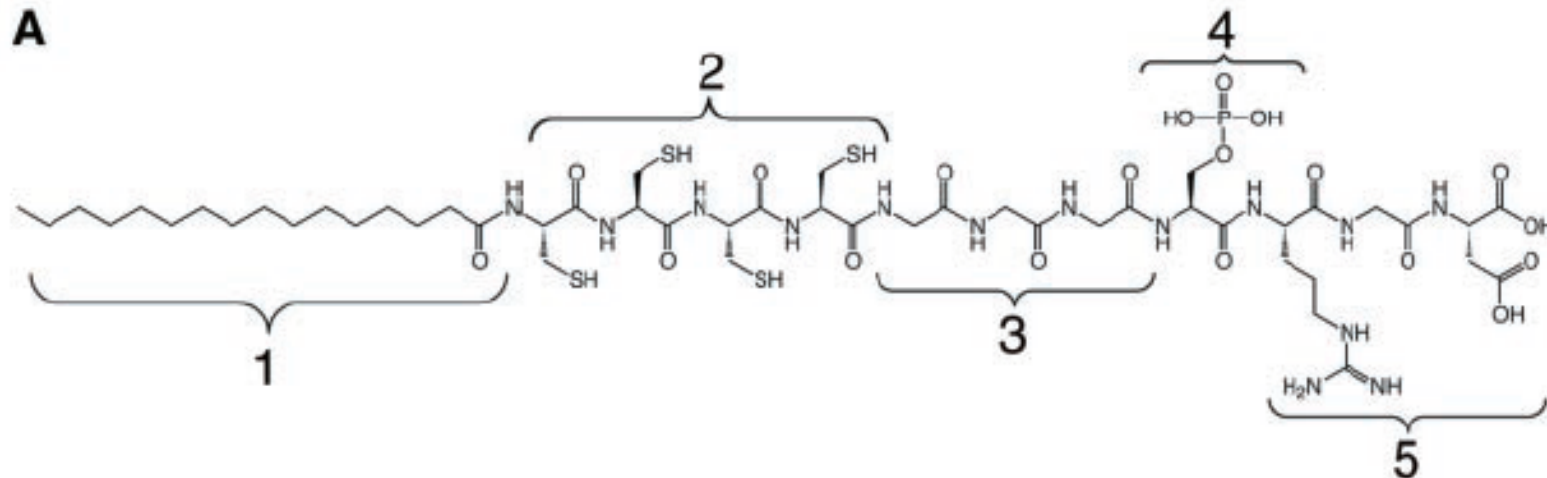
- 1 hydrophobic alkyl tail
- 2 four cysteine residues for SS cross-linking
- 3 flexible triglycine linker region
- 4 phosphorylated serine for Ca^{++} binding & hydroxyapatite crystal organization
- 5 cell adhesion ligand Arg-Gly-Asp (RGD)

Mineralization

Fig. 2. (A) Negative stain (phosphotungstic acid) TEM of the self-assembled nanofibers before covalent capture. Fibers are arranged in ribbon-like parallel arrays. (B) Vitreous ice cryo-TEM of the fibers reveals the diameter of the fibers in their native hydrated state to be 7.6 ± 1nm. (C) Positive stain (uranyl acetate) TEM of the self-assembled nanofibers after oxidative cross-linking shows electron dense regions due to the stain that localized on the periphery of the fibers. (D) Thin section TEM of positively stained (uranyl acetate) nanofibers after oxidative cross-linking and embedding in epoxy resin. Two fibers are observed in cross section (arrows), showing the lack of staining in the interior of the fiber.
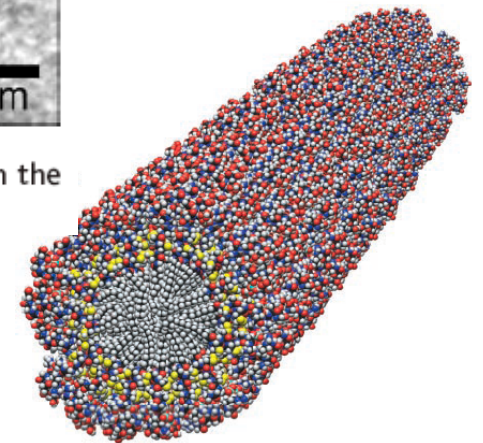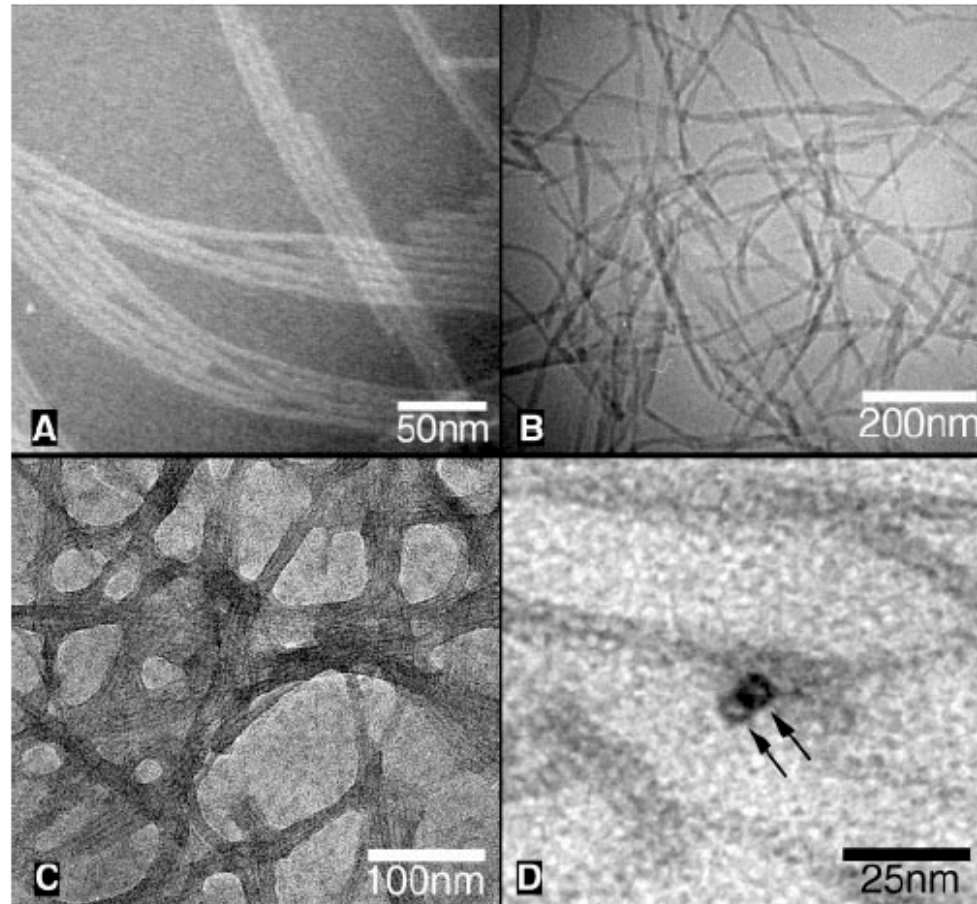
Mineralization

Fig. 4. Scheme showing relations between peptide-amphiphile fibers and hydroxyapatite crystals in the mineralized bundle. Arrow indicates the direction of the c axes of the crystals.

c - axis

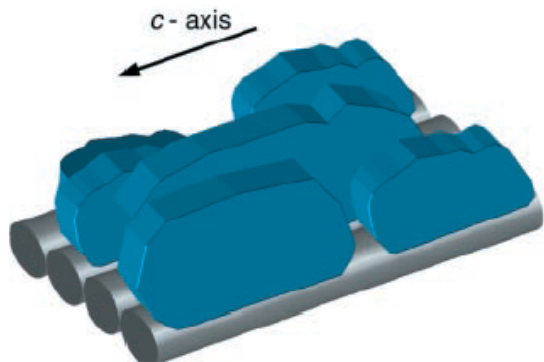Fig. 3. (A) TEM micrographs of the unstained, cross-linked peptide-amphiphile fibers incubated for 10 min in $CaCl_2$ and Na_2HPO_4 solution. The fibers arranged in bundles are visible due to the high concentration of inorganic ions on their surface. (B) After 20 min, forming HA crystals (red arrows) are observed in parallel arrays on some of the PA fibers. (C) After 30 min, mature HA crystals (red arrows) completely cover the PA fibers. (D) Electron diffraction pattern taken from a mineralized bundle of PA fibers after 30 min of exposure to calcium and phosphate. The presence and orientation of the diffraction arcs corresponding to the 002 and 004 planes (whose intensities are enhanced with respect to the 211 family of reflections) indicate preferential alignment of the crystals with their c axes along the long axis of the bundle. (E) Plot of intensity versus inverse angstroms reveals that the 002 and 004 peaks of hydroxyapatite are strongly enhanced along the peptide-amphiphile fiber axis. (F) EDS profile of mineral crystals after 30 min of incubation reveals a Ca/P ratio of 1.67 ± 0.08, as expected for HA.
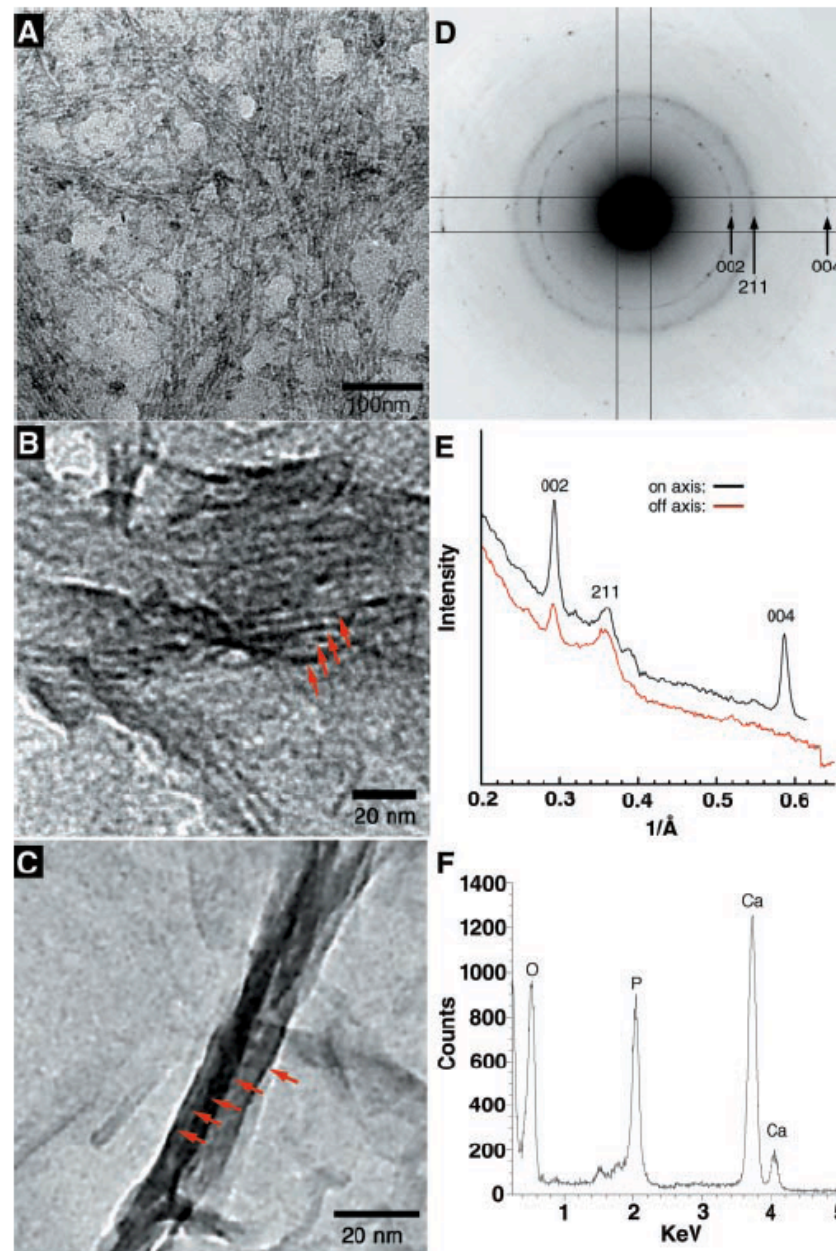
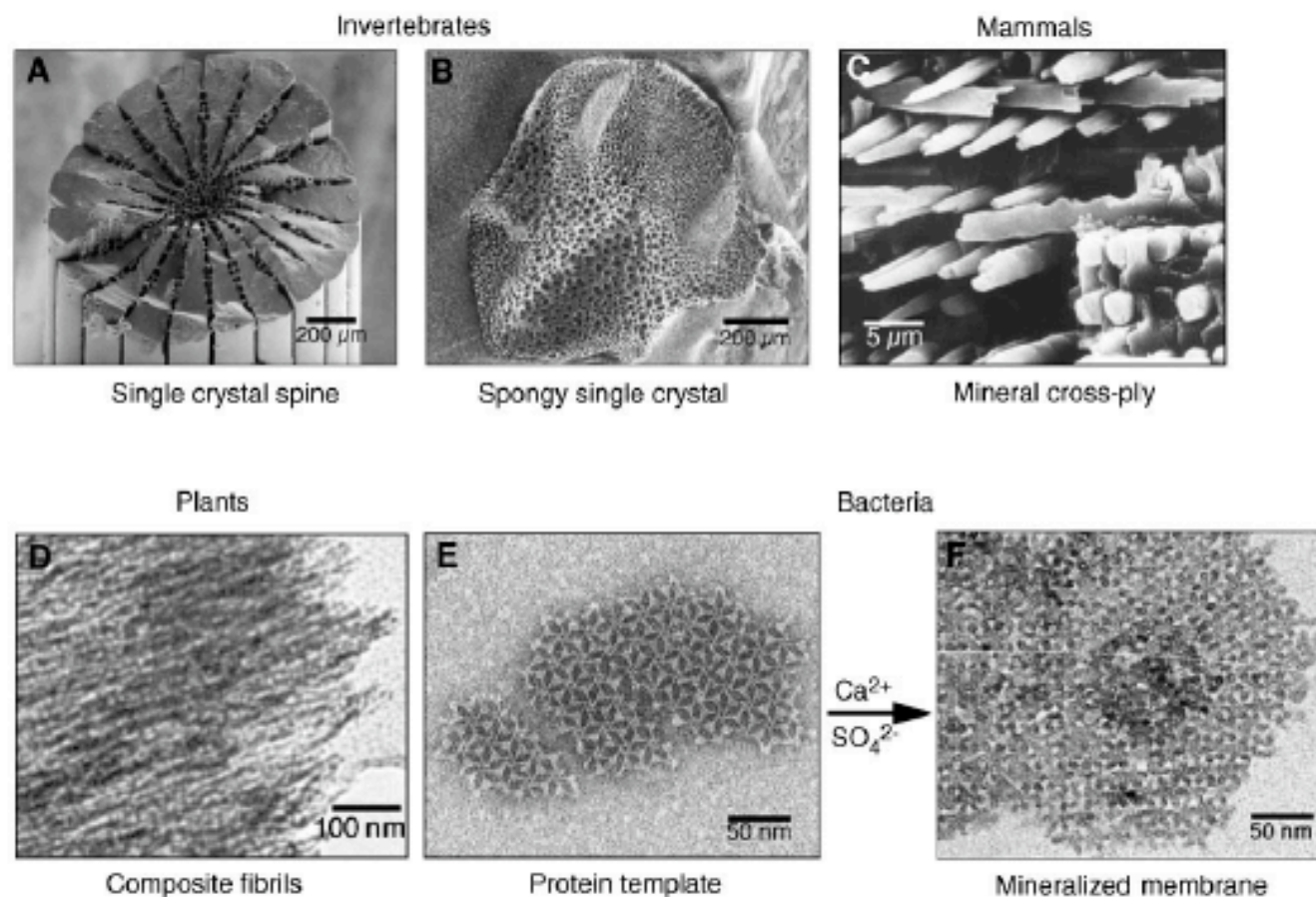# Molecular Manipulation of Microstructures: Biomaterials, Ceramics, and Semiconductors

Samuel I. Stupp* and Paul V. Braun

Organic molecules can alter inorganic microstructures, offering a very powerful tool for the design of novel materials. In biological systems, this tool is often used to create microstructures in which the organic manipulators are a minority component. Three groups of materials—biomaterials, ceramics, and semiconductors—have been selected to illustrate this concept as used by nature and by synthetic laboratories exploring its potential in materials technology. In some of nature's biomaterials, macromolecules such as proteins, glycoproteins, and polysaccharides are used to control nucleation and growth of mineral phases and thus manipulate microstructure and physical properties. This concept has been used synthetically to generate apatite-based materials that can function as artificial bone in humans. Synthetic polymers and surfactants can also drastically change the morphology of ceramic particles, impart new functional properties, and provide new processing methods for the formation of useful objects. Interesting opportunities also exist in creating semiconducting materials in which molecular manipulators connect quantum dots or template cavities, which change their electronic properties and functionality.

Stupp

Invertebrates

A Single crystal spine

B Spongy single crystal

Mammals

C Mineral cross-ply

Plants

D Composite fibrils

E Protein template

Bacteria

Ca^{2+}
SO_4^{2-}

F Mineralized membrane

Fig. 1. Electron micrographs of molecularly manipulated inorganic microstructures observed in nature. Two unusual calcite single crystals are observed in invertebrates: one is a spine with radial texture in the sea urchin (**A**) and the other is a sponge with different size pores in the arm of the star *Ophiocoma wendti* (**B**) (*1*) (reproduced by permission of the Royal Society of Chemistry). An example from mammals is observed in the incisor of a rat, which generates crossed elongated crystals of carbonated apatite reminiscent of an advanced composite microstructure (**C**) (*1*) (reproduced by permission of the Royal Society of Chemistry). In certain plants, macromolecules can stabilize amorphous silica with a specific morphology (**D**) [reproduced from (*13*) with kind permission from Elsevier Science Ltd, the Boulevard, Langford Lane, Kidlington OX5 1GB, UK], and in the membrane of some bacteria, they form highly symmetric templates for mineralization (**E** and **F**) [reproduced with permission from (*17*)].

Stupp

A

B
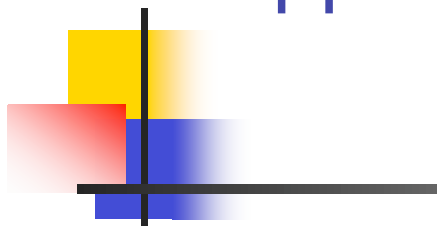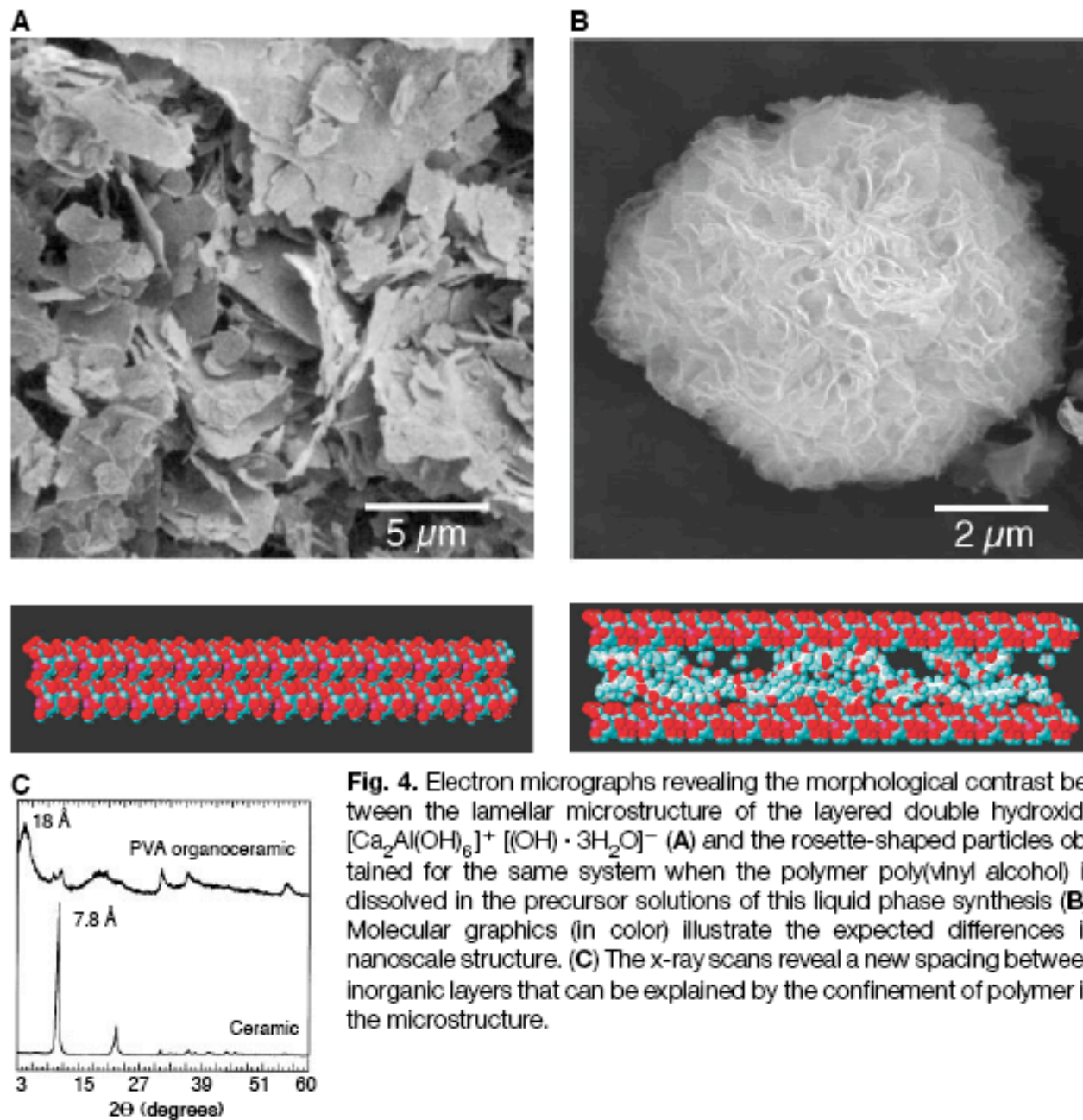
Change
polypeptide
change
crystalline
form.
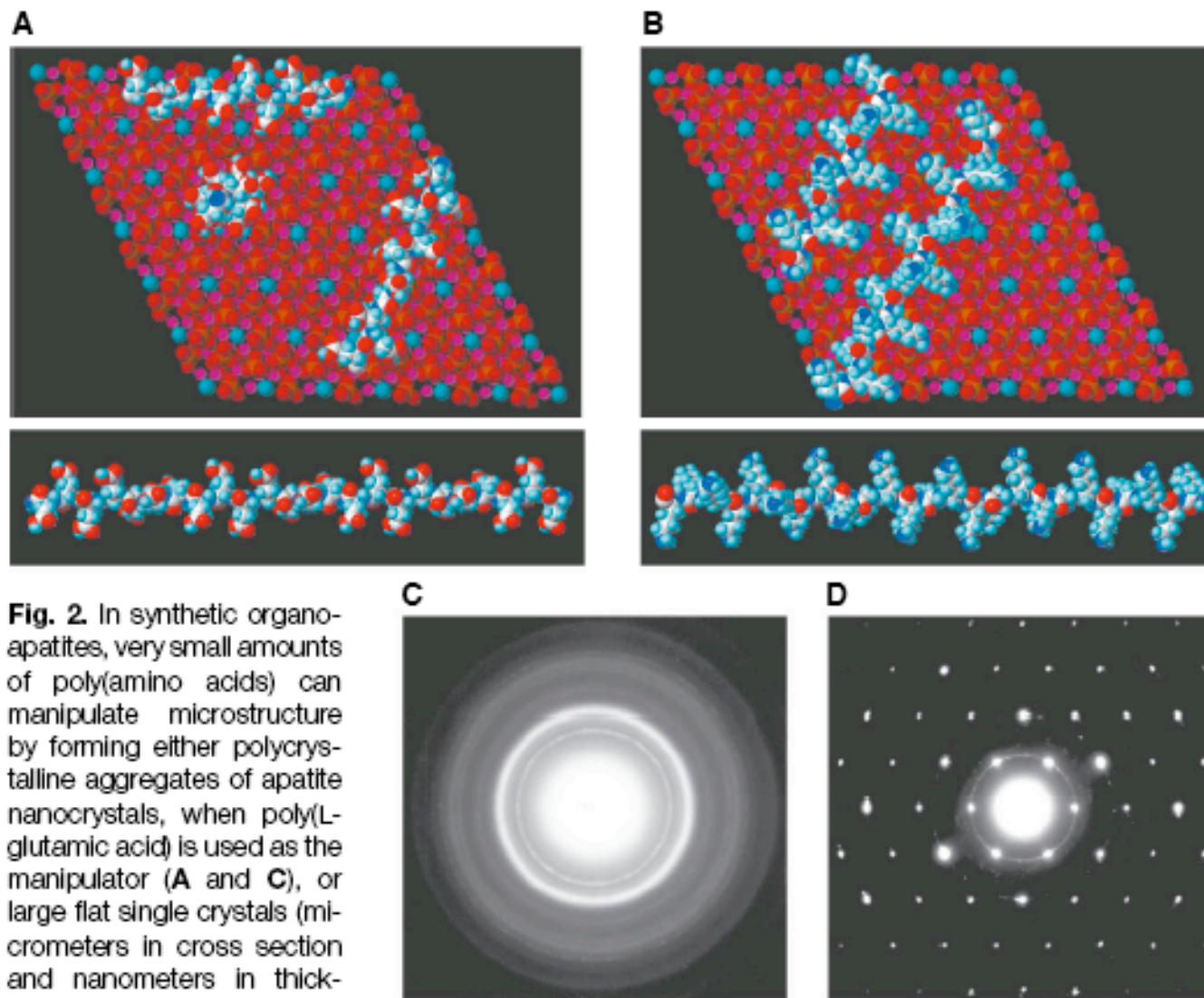
Fig. 2. In synthetic organo-apatites, very small amounts of poly(amino acids) can manipulate microstructure by forming either polycrystalline aggregates of apatite nanocrystals, when poly(L-glutamic acid) is used as the manipulator (**A** and **C**), or large flat single crystals (micrometers in cross section and nanometers in thickness), when poly(L-lysine) is present in the mother liquor (**B** and **D**). Note the coherence between the apatite crystal lattice and the amino groups of the poly(L-lysine) chain in (B).

C

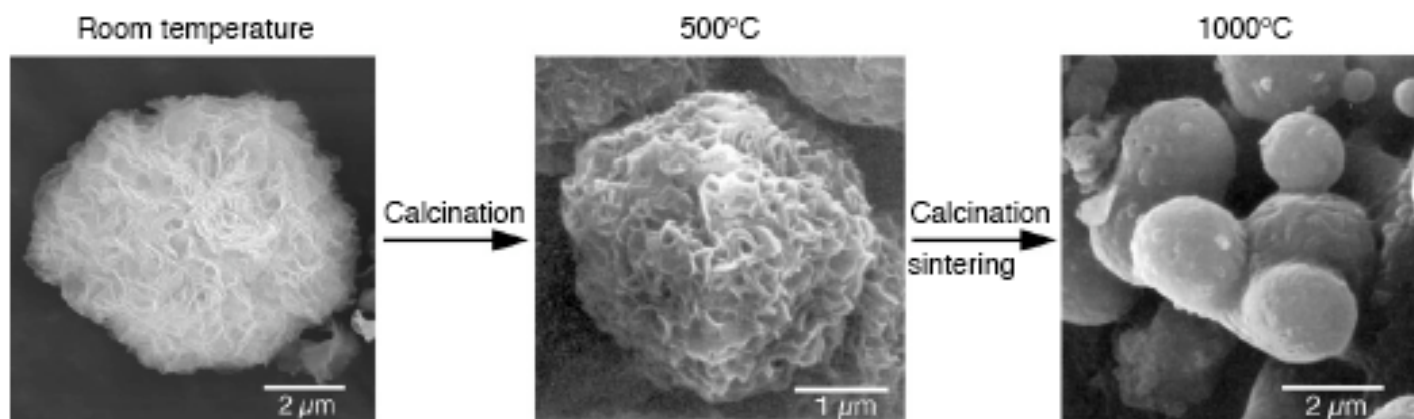**D**

4/25/06   LaBean COMPSCI 296.5

Stupp

Add organic component change micro- structure.

A

B

5 μm

2 μm

C

18 Å

PVA organoceramic

7.8 Å

Ceramic

3   15   27   39   51   60
2Θ (degrees)

Fig. 4. Electron micrographs revealing the morphological contrast between the lamellar microstructure of the layered double hydroxide $[Ca_2Al(OH)_6]^+$ $[(OH) \cdot 3H_2O]^-$ (**A**) and the rosette-shaped particles obtained for the same system when the polymer poly(vinyl alcohol) is dissolved in the precursor solutions of this liquid phase synthesis (**B**). Molecular graphics (in color) illustrate the expected differences in nanoscale structure. (**C**) The x-ray scans reveal a new spacing between inorganic layers that can be explained by the confinement of polymer in the microstructure.

4/25/06

Stupp

Room temperature   500°C   1000°C

Calcination

Calcination sintering

2 μm   1 μm   2 μm

Fig. 5. The morphology of inorganic-organic composite particles is preserved as the system is calcined to form a mostly inorganic material (500°C), and the particle's spheroidal contour is still observed as the organic content vanishes and the material transforms to ceramic by 1000°C.

Physical and chemical treatments of composites can have differential effects on organic and inorganic components.

Stupp

Molecular
manipulation of
microstructures
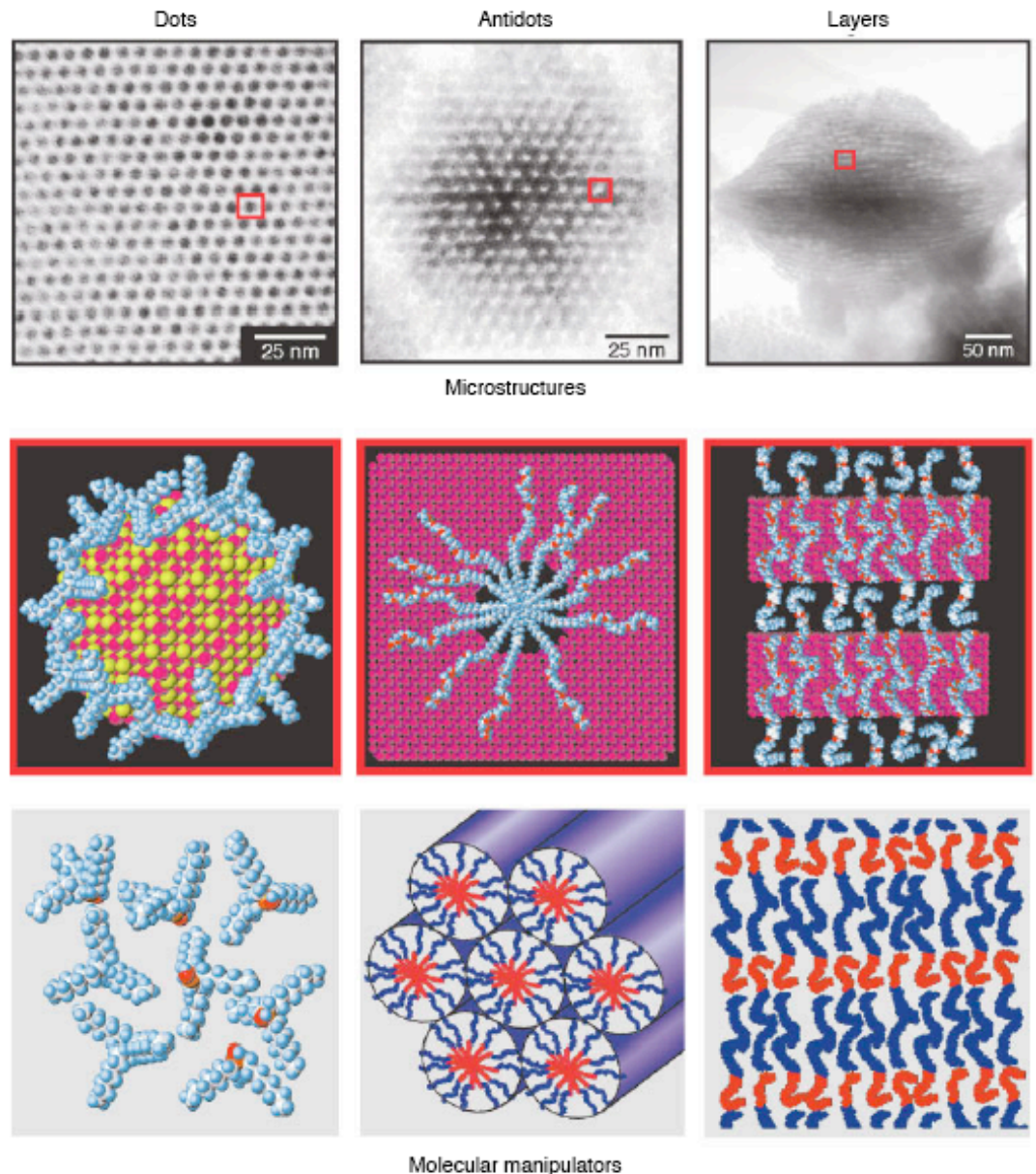
Fig. 6. Transmission electron micrographs of three molecularly manipulated microstructures of II-VI semiconductors: a colloidal crystal of CdSe nanocrystals covered by organic surfactants, a colloid of $Cd_{(1-x)}Zn_xS$ punctured by a regular array of cavities templated by cylindrical molecular assemblies of surfactant molecules, and a lamellar particle with alternating CdS and organic layers templated by an organic lamellar mesophase. Below the micrographs, models and schematic representations of the hybrid structures and their respective molecular manipulators are shown in color.

4/25/06

Biomimetic synthesis of ordered silica structures mediated by block copolypeptides

Jennifer N. Cha[*], **Galen D. Stucky**[†*], **Daniel E. Morse**[‡] **& Timothy J. Deming**[†*]

*Departments of * Chemistry, † Materials, and ‡ Molecular, Cellular and Developmental Biology, University of California, Santa Barbara, California 93106. USA*

**Table 1 Block copolypeptides screened for their ability to react with TEOS to form silica**

| Block copolymer	Composition	Synthesis yield (%)	SiO$_2$ rate	
			N$_2$	Air
1	poly(L-alanine$_{30}$-b-L-lysine$_{200}$)	87	0.09(2)	NA
2	poly(L-glutamine$_{30}$-b-L-lysine$_{200}$)	88	0.22(7)	NA
3	poly(L-serine$_{30}$-b-L-lysine$_{200}$)	84	0.29(3)	NA
4	poly(L-tyrosine$_{30}$-b-L-lysine$_{200}$)	86	0.30(7)	NA
5	poly(L-cysteine$_{10}$-b-L-lysine$_{200}$)	76	0.60(2)	0.60(2)
6	poly(L-cysteine$_{30}$-b-L-lysine$_{200}$)	77	0.43(2)	0.62(4)
7	poly(L-cysteine$_{60}$-b-L-lysine$_{200}$)	87	0.37(4)	0.67(1)
8	poly(L-cysteine$_{30}$-b-L-lysine$_{400}$)	88	0.62(1)	0.65(4)
9	poly(L-cysteine$_{30}$-b-L-glutamate$_{200}$)	90	0.01(1)	0.01(1)
10	poly(L-cysteine$_{30}$)	76	0.43(6)	0.08(1)
11	poly(L-lysine$_{200}$)	96	0.01(1)	NA
12	none	NA	0.01(1)	NA

tetraethoxysilane (TEOS)
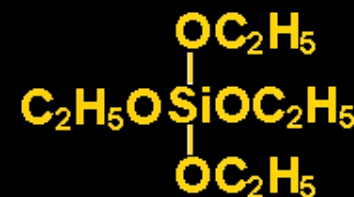
Block co-polymer, silica
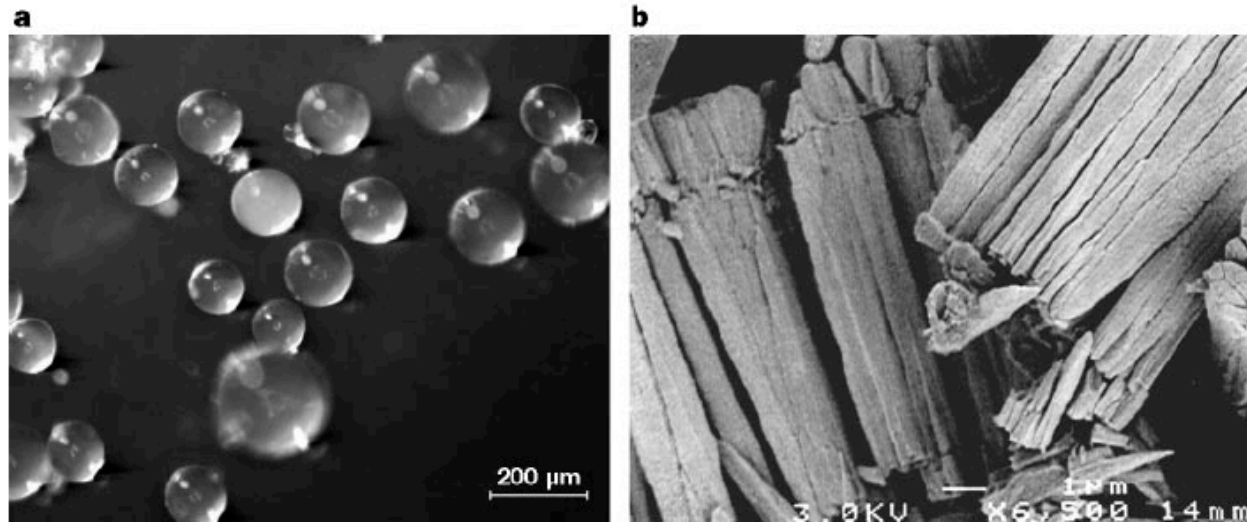
Figure 2 Different ordered silica shapes obtained using block copolypeptide **6**. In a typical procedure, TEOS (2.0 ml) was added to 500 μl of a solution of **6** (5 mg ml^{-1} in 50 mM Tris-HCl buffer, pH 6.8), and the resulting biphasic mixture was agitated vigorously and then allowed to stand for several hours with no stirring, whereupon some of the TEOS had emulsified into the aqueous phase. After 24 h, the resulting silica precipitate was collected from the aqueous phase, washed with 95% ethanol and air dried. **a**, Optical micrograph of silica spheres obtained from synthesis under nitrogen; scale bar, 200 μm. **b**, Scanning electron micrograph of packed silica columns obtained from synthesis under air; scale bar, 1 μm. The sample was sputter coated with gold and examined with a JEOL JSM 6300F equipped with a cold cathode field-emission source operated at a beam energy of 3.0 kV.
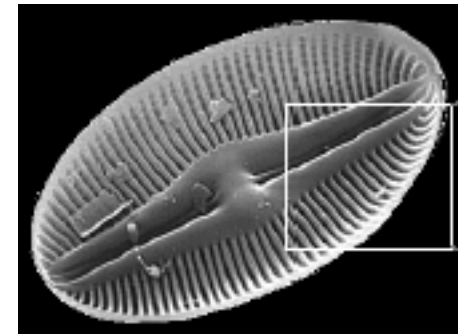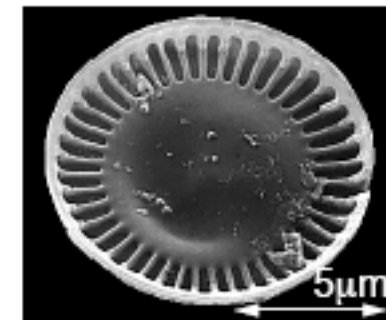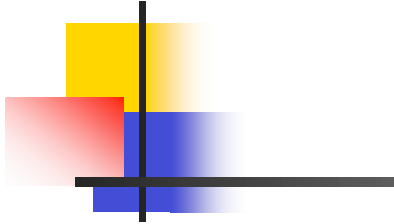
Diatoms
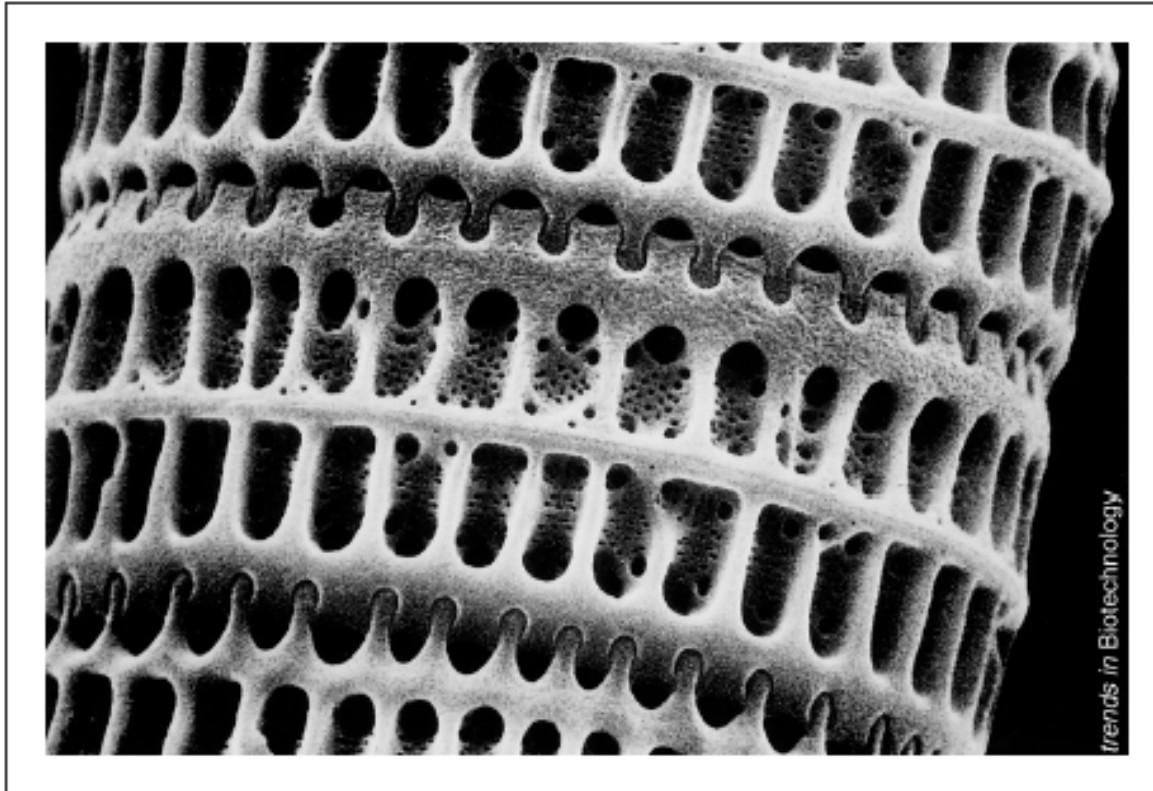
Figure 1
Genetically controlled nanoscale architecture of the silica wall of the marine diatom *Paralia sulcata* (30 μm in diameter). (Electron micrograph by G. Hallegraeff;

- **Silica**
  - $(SiO_2)_n$
- **Silicic acid**
  - $Si(OH)_4$

Polycationic Peptides from Diatom Biosilica That Direct Silica Nanosphere Formation

Nils Kröger,* Rainer Deutzmann, Manfred Sumper

Diatom cell walls are regarded as a paradigm for controlled production of nanostructured silica, but the mechanisms allowing biosilicification to proceed at ambient temperature at high rates have remained enigmatic. A set of polycationic peptides (called silaffins) isolated from diatom cell walls were shown to generate networks of silica nanospheres within seconds when added to a solution of silicic acid. Silaffins contain covalently modified lysine-lysine elements. The first lysine bears a polyamine consisting of 6 to 11 repeats of the N-methyl-propylamine unit. The second lysine was identified as ε-N,N-dimethyl-lysine. These modifications drastically influence the silica-precipitating activity of silaffins.

- Polycationic peptides (silaffins) with modified lysine residues.

Diatoms, peptide, silica

Fig. 1. Ultrastructure of *C. fusiformis* cell wall analyzed by transmission electron microscopy (TEM). (**A**) Isolated cell wall. Rows of parallel silica strips are running in a helical mode along the longitudinal axis of the cell. Bar: 2.5 μm. (**B** and **C**) Details of a *C. fusiformis* cell in cross section. The arrowheads indicate the position of the plasma membrane and point toward the extracellular space. Bars: 100 nm. (B) Lateral region. Each oval-shaped element represents a single silica strip of the cell wall in cross section. The arrow indicates a nascent silica strip within its SDV shortly before secretion. (C) Valve region. The ringlike structure and the two oval-shaped elements on either side are silicified cell wall elements.
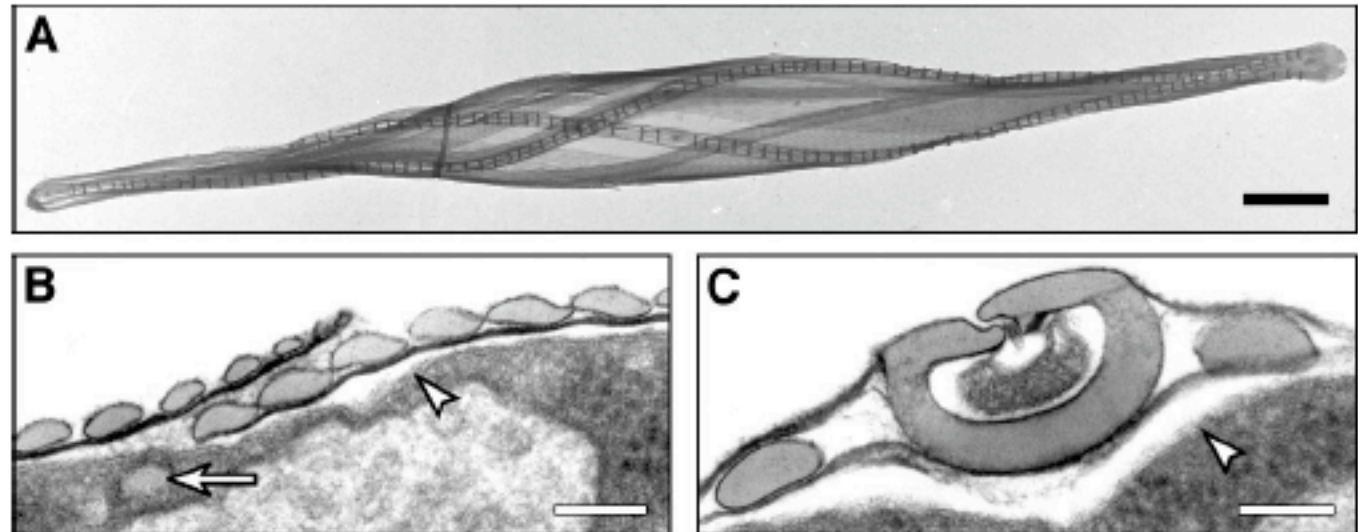
Diatoms, peptide, silica

SSXX'SGSYSG(S/Y)
SSXX'SGSYYSYGT

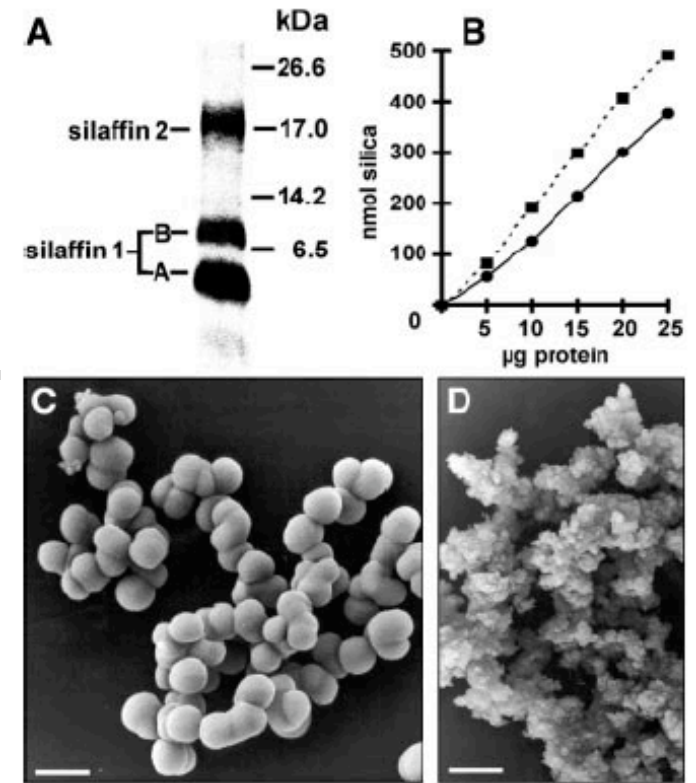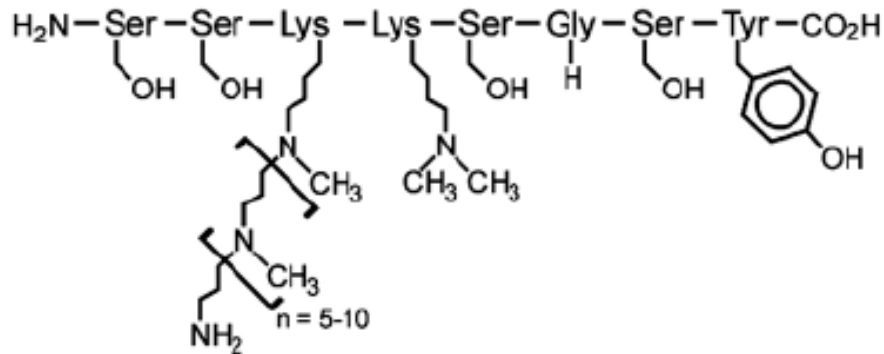$H_2N-Ser-Ser-Lys-Lys-Ser-Gly-Ser-Tyr-CO_2H$

n = 5-10

Fig. 2. Silica precipitation induced by silaffins (14). (A) Low molecular mass fraction of HF extract from *C. fusiformis* cell walls. The extract was subjected to Tricine–SDS-PAGE (13) and stained with Coomassie blue. (B) Correlation between silaffin concentration (27) and the amount of silica precipitated from a silicic acid solution. The dotted line represents the result obtained for the silaffin mixture; the solid line shows the result for pure silaffin-1A (15). (C and D) SEM micrographs of silica precipitated by silaffin-1A (C) and the mixture of silaffins (D). The diameter of silica particles is 500 to 700 nm (C) and <50 nm (D). The protein concentration was 5 mg/ml. Bar: 1 μm.

Ultrafast holographic nanopatterning of biocatalytically formed silica

Lawrence L. Brott*, Rajesh R. Naik*, David J. Pikas*, Sean M. Kirkpatrick*, David W. Tomlin*, Patrick W. Whitlock*†, Stephen J. Clarson† & Morley O. Stone*

* Materials and Manufacturing Directorate, Air Force Research Laboratory, 3005 P Street, Wright-Patterson Air Force Base, Ohio 45433-7702, USA
† Department of Materials Science and Engineering, University of Cincinnati, 497 Rhodes Hall, Cincinnati, Ohio 45221-0012, USA
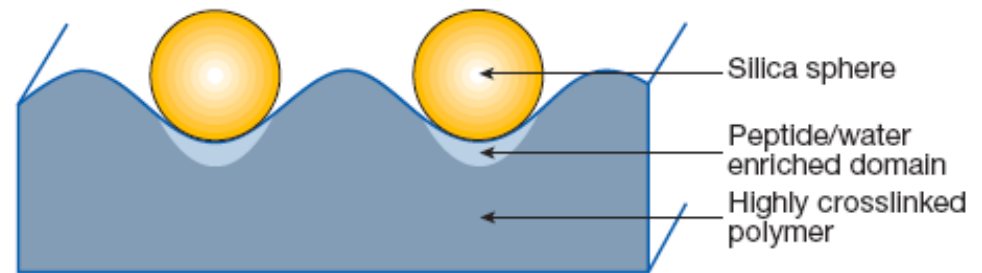
Figure 1 Cross-section of the hologram. The peptide-rich regions that are formed during the holographic polymerization process are shown.

- Diatoms (microscopic, single-celled algae) create intricate, highly complex silica structures under physiological conditions.

- Synthetic attempts have required extreme laboratory conditions.

silica

Table 1 Properties of holograms with and without silica nanospheres

	Hologram with silica	Hologram without silica
Grating spacing	1.60 μm	1.33 μm
Diffraction efficiency	0.95%	0.019%
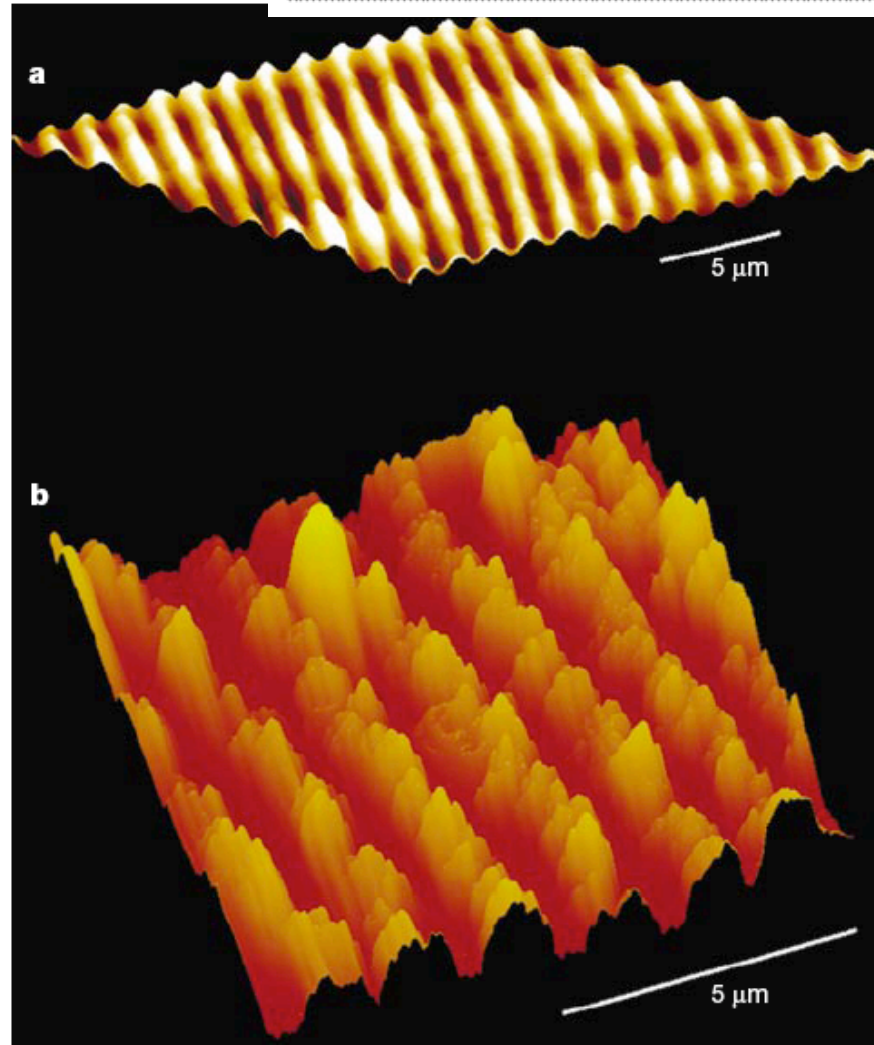
Figure 2 Surface relief pattern of the cured polymer. Atomic force microscope images of the control polymer before silification (**a**) and the hybrid structure after silification (**b**).
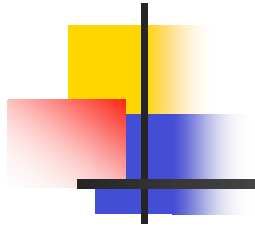
silica
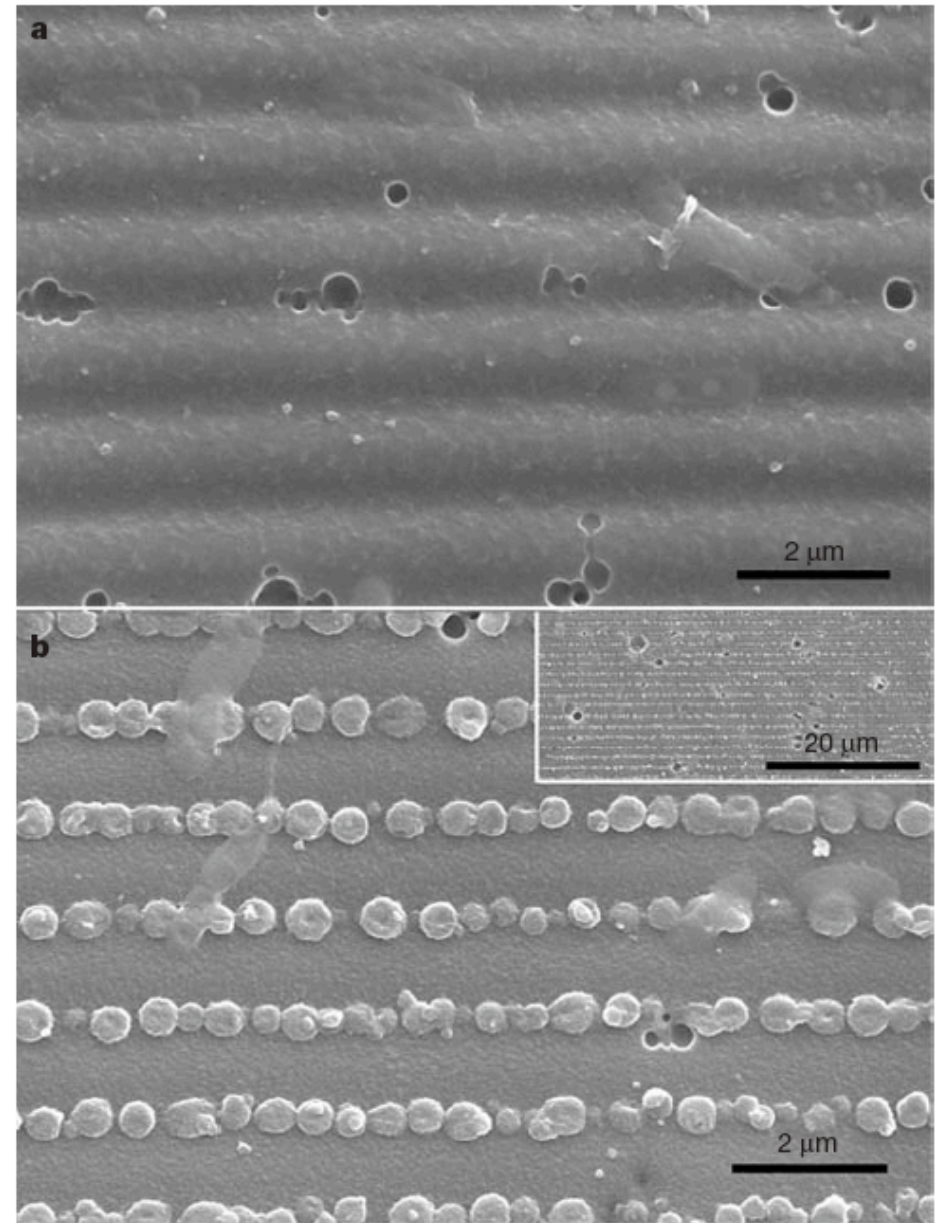
Figure 3 Two-dimensional array of ordered silica nanospheres formed within the hologram. Scanning electron microscope images of the control hologram after being treated with the liquid silane (**a**) and the biosilica nanostructure created by reacting the silane with a peptide-embedded hologram (**b**).

- Blah
- Blah

LaBean COMPSCI 296.5